Photoacoustics 26 (2022) 100348

Contents lists available at ScienceDirect

Photoacoustics

journal homepage: www.elsevier.com/locate/pacs

Photoacoustic imaging phantoms for assessment of object detectability and boundary buildup artifacts

Jorge Palma-Chavez [a], Keith A. Wear [b], Yash Mantri [c], Jesse V. Jokerst [a,d,e,*], William C. Vogt [b,**]

[a] Department of NanoEngineering, University of California San Diego, La Jolla, CA 92093, USA
[b] Center for Devices and Radiological Health, US Food and Drug Administration, Silver Spring, MD 20993, USA
[c] Department of Bioengineering, University of California, San Diego, La Jolla, CA 92093, USA
[d] Department of Radiology, University of California San Diego, La Jolla, CA 92093, USA
[e] Material Science Program, University of California San Diego, La Jolla, CA 92093, USA

ARTICLE INFO

Keywords:
Tissue-mimicking material
Phantoms
Polyacrylamide
Image quality
3D printing
Standardization

ABSTRACT

Standardized phantoms and test methods are needed to accelerate clinical translation of emerging photoacoustic imaging (PAI) devices. Evaluating object detectability in PAI is challenging due to variations in target morphology and artifacts including boundary buildup. Here we introduce breast fat and parenchyma tissue-mimicking materials based on emulsions of silicone oil and ethylene glycol in polyacrylamide hydrogel. 3D-printed molds were used to fabricate solid target inclusions that produced more filled-in appearance than traditional PAI phantoms. Phantoms were used to assess understudied image quality characteristics (IQCs) of three PAI systems. Object detectability was characterized vs. target diameter, absorption coefficient, and depth. Boundary buildup was quantified by target core/boundary ratio, which was higher in transducers with lower center frequency. Target diameter measurement accuracy was also size-dependent and improved with increasing transducer frequency. These phantoms enable evaluation of multiple key IQCs and may support development of comprehensive standardized test methods for PAI devices.

1. Introduction

Photoacoustic imaging (PAI) has shown great potential to provide additional molecular and functional biomarkers for various clinical applications including cancer detection, vascular imaging, tissue oximetry, and biopsy/surgical guidance [1–7]. The broad range of applications with substantially different requirements has resulted in a wide variety of system designs [8]. Accurately predicting how these differences in design parameters influence PAI device performance in vivo can be challenging. However, phantom-based test methods can provide insight on design consequences and help set performance expectations and limitations. Thus, tissue-mimicking phantoms provide an important approach for objective, quantitative evaluation of fundamental image quality characteristics (IQCs), enabling device design optimization, calibration, constancy testing, and regulatory decision-making.

An ideal tissue-mimicking material (TMM) for PAI phantoms would simultaneously possess optical and acoustic properties that are both tunable and biologically relevant. PAI phantoms have been fabricated using many materials, including paraffin gel wax;[9,10] emulsions such as Intralipid [11] and glycerol-in-polydimethylsiloxane;[12] polyvinyl chlorine plastisol (PVCP);[13–16] copolymer-in-oil;[17,18] and hydrogels such as gelatin [19], agar/agarose [20–25], and polyvinyl alcohol [26–28]. Promising PVA and PVCP TMMs have been reported for the preparation of breast-mimicking phantoms. PVA TMMs with adjustable stiffness and turbidity are prepared by repeated freeze-thaw cycling [27]. However, the optical and acoustic properties cannot be tuned independently, and dye diffusion within the TMM has been reported [28]. PVCP TMMs offer high optical and acoustic tunability as well as temporal stability [15], and complex solid inclusions can also be formed [16,29]. However, PVCP requires preparation at high temperatures, potentially limiting the compatible materials used for phantom molding as well as imaging target options.

We recently developed a polyacrylamide (PAA) TMM that offers simple and fast preparation, greater mechanical strength and longer shelf life than agar/gelatin hydrogels, lower preparation temperatures than PVCP and gel wax, and high optical tunability [30]. However, this

* Corresponding author at: Department of NanoEngineering, University of California San Diego, La Jolla, CA 92093, USA.
** Corresponding author.
E-mail addresses: jjokerst@ucsd.edu (J.V. Jokerst), william.vogt@fda.hhs.gov (W.C. Vogt).

https://doi.org/10.1016/j.pacs.2022.100348
Received 5 November 2021; Received in revised form 18 February 2022; Accepted 17 March 2022
Available online 21 March 2022

TMM had a relatively high speed of sound (1540 m/s) and fairly low acoustic attenuation compared to some tissues, especially breast [30–32]. In PAA and most available TMMs, achieving high acoustic tunability is often more challenging than achieving optical tunability, which can limit the tissue types that can be simulated. To overcome these limitations, liquid additives such as mineral oil [33], glycerol [34] or ethylene glycol [35] can be added to modify the TMM's speed of sound, while solid additives such as alumina [34,36], glass beads [37–39], or silica particles [33] have been shown to increase the acoustic attenuation (mostly by increasing scattering).

In addition to well-characterized TMMs, it is equally important to carefully design reproducible phantom geometries, target inclusion sizes and patterns, and image acquisition and analysis protocols. We recently reviewed common practices in PAI phantom design and testing, and compared them to standardized IQC test methods used for mature imaging modalities [40]. Several understudied IQCs were identified, including: size-dependent low-contrast object detectability; geometric accuracy (the ability to accurately represent real dimensions of imaged features); and artifacts. One critical artifact to consider is boundary buildup, a well-known bandlimited sensing artifact where only edges of absorptive objects are visualized by PAI [41]. Our review suggested that these IQCs may be understudied due to the absence of adequate or well-accepted phantom designs to assess them.

Imaging target selection is another major consideration for phantom design. Ideally, imaging targets would be solid inclusions made of tunable TMM, which could be prepared with variable shapes and dimensions, and could represent small assemblies of small absorbers (e.g., arterioles and capillaries). Most reported PAI phantoms use tubes or wall-less channels filled with contrast media such as dyes, blood, or nanoparticles [29,30,40,42]. However, tubes are often only available in relatively large sizes representative of larger blood vessels, rather than smaller vasculature. For both large and small tubes, the walls may potentially alter photoacoustic signals and light and sound transport effects. Additionally, the use of tubes requires phantom housing connectors or adhesives, and well as requiring contrast media injection and phantom cleaning for every imaging session. While flow channel phantoms allow rapid adjustment of inclusion properties, they carry the increased costs of flow loop equipment. With water-based TMMs such as polyacrylamide hydrogel, the injection of hydrophilic contrast media through wall-less channels would be inappropriate as it would readily diffuse into the hydrogel material. Similarly, wall-less channel PVCP phantoms can be difficult to keep clean with repeated use, and tubing may only partially alleviate this issue. Also, using blood elevates safety concerns during phantom use, and blood is not strictly needed for general image quality assessment as generic black dyes are suitable for this purpose [43]. Nanoparticles are generally expensive and may also suffer photodamage with repeated imaging, degrading imaging phantom stability and repeatability [44].

Semi-anthropomorphic breast phantoms have been recently reported for PAI [16,29]. These phantoms are composed of multiple layers of PVCP breast-mimicking TMMs embedding spherical inclusions and wall-less channels for absorber injection. Although anthropomorphic phantoms can produce more life-like image features, image quality phantoms generally rely on idealized targets such as cylinders and spheres for objective, quantitative image quality assessment [40]. This latter phantom paradigm is more consistent with standardized phantom-based image quality test methods for mature modalities such as CT, mammography, MRI, and ultrasound.

Our overall goal was to develop stable, tunable, and well-characterized breast-mimicking phantoms to enable evaluation of understudied IQCs in PAI phantom testing. To this end, our study objectives were to: 1) develop tunable PAA-based TMMs to mimic breast fat and parenchyma tissues, 2) fabricate solid PAA imaging targets with adjustable properties and geometry, and 3) design a multi-purpose phantom for evaluation of understudied IQCs such as object detectability, geometric accuracy, and boundary buildup artifact vs. target size, depth, and optical properties. To the best of our knowledge, these are the first well-characterized image quality phantom targets prepared with a TMM that generates "filled-in" PAI features. Similarly, the phantom designs and test methods proposed here are a first attempt to evaluate understudied PAI IQCs we previously identified through literature review [40]. Finally, to encourage adoption of the phantoms proposed in this study, all 3D-printer designs are readily available through the NIH 3D-File Exchange website [45].

2. Methods

2.1. TMM production

TMMs for PAI phantoms should offer highly tunable optical and acoustic properties in order to adequately mimic different tissue types and compositions. In this study, we aimed to produce TMMs capable of mimicking breast fat tissue (denoted F-TMM) and parenchyma tissue (P-TMM), as well as a target TMM (T-TMM) for producing imaging targets that resemble clusters of sub-resolution vasculature. Target optical absorption coefficient (μ_a) at 850 nm was 0.1 cm^{-1}, and target optical reduced scattering coefficients (μ_s') at 850 nm were 8 and 10 cm^{-1} for fat and parenchyma, respectively [46–48]. Target speed of sound (c_s) values were 1430 and 1540 m/s, and frequency derivatives ($d\alpha/df$) of target acoustic attenuation (α) were 0.6 and 2.5 dB/cm/MHz for fat and parenchyma, respectively [31,32,49–52].

To enhance the acoustic tunability of our previously developed PAA TMM [30], we created emulsion-based hydrogels by adding silicone oil (XIAMETER™ PMX-0210, Dow, Inc., Midland, MI) and/or ethylene glycol (324558, Sigma-Aldrich, Inc., St. Louis, MO) [53]. Silicone oil was selected over other oils such as mineral oil and turpentine due to its significantly lower speed of sound (1040 m/s) and its broad availability in different viscosities. Fig. 1 illustrates our developed TMM preparation process. Briefly, an oil-in-water (O/W) emulsion was formed by adding silicone oil to a solution of deionized water, Tween 20 surfactant (P1379, Sigma-Aldrich), and ethylene glycol. Oil was dispersed into suspended droplets using either a tissue homogenizer (985370–14, BioSpec, Bartlesville, OK) or a probe sonicator (Q125, Qsonica, Newtown, CT). The emulsion was transferred into a vacuum chamber and degassed for 30 min. After degassing, a 40% w/v acrylamide solution containing 19:1 acrylamide:bisacrylamide (AM9024, Thermo Fisher Scientific, Inc., Waltham, MA) was added to the emulsion. N,N,N', N'-tetramethylethylenediamine (TEMED, T9281, Sigma-Aldrich, Inc.) was added to accelerate free radical formation, and finally ammonium persulfate (APS) solution (A7460, Sigma-Aldrich, Inc.) was added to initiate polymerization. The solution was then immediately poured into various molds (Section 2.3), which typically solidified for 5–20 min depending on the total mass.

To study the effect of silicone oil concentration on TMM properties, silicone oil with viscosity of 100 centistokes (cSt) was added at 6–26% w/w of total TMM mass and probe sonicated for two minutes at 50% amplitude, 75% duty cycle. The effect of emulsification intensity was studied by varying the amplitude/speed of either a homogenizer or a probe sonicator from 50% to 100%, and emulsifying TMMs containing silicone oils with viscosities of 100 and 350 cSt. The effect of the duration of the emulsification process was studied by varying emulsification time of a 1000 cSt silicone oil emulsion from 2 to 10 min using 100% probe sonication amplitude.

To adjust TMM optical properties, India ink (Super black India ink, Speedball Art Products Co., NC), alcohol soluble Nigrosin (211680, Sigma-Aldrich, Inc.), and anatase titanium dioxide (TiO_2, 232033, Sigma-Aldrich, Inc.) were added. India ink was suspended in the TMM's water phase at concentrations from 0.006% to 0.06% w/w. Nigrosin powder was suspended in 100 cSt silicone oil, bath sonicated for 20 min, and added to the TMM as described above. Nigrosin concentration was varied from 0.01% to 0.1% w/w of the final TMM's mass. Optical scattering was controlled by adding TiO_2 particles to the water phase at

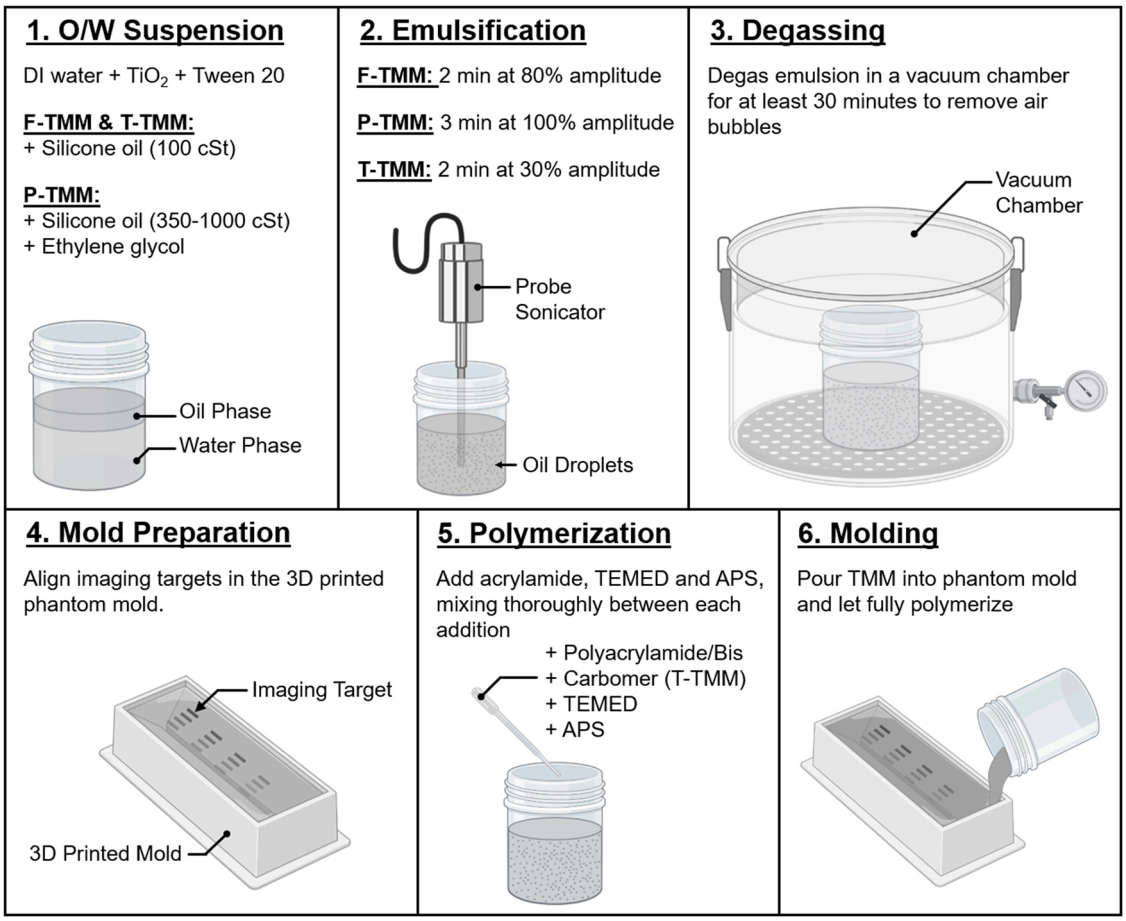

Fig. 1. Step-by-step preparation of emulsion-based TMMs for breast fat (F-TMM), parenchyma (P-TMM), and imaging targets (T-TMM).

0.01–0.1% w/w. Carbomer 940 (C1477, Spectrum, New Brunswick, NJ) was used to enhance mechanical strength of TMM formulations intended as solid imaging targets, thus allowing the use of injection molding techniques [54]. Carbomer was dissolved in DI water and added to the TMM after emulsification from 0.05% to 0.3% w/w.

2.2. TMM characterization

TMM speed of sound and acoustic attenuation vs. frequency were characterized using a broadband through-transmission substitution technique as described previously [30]. TMM optical absorption coefficient and reduced scattering coefficient were measured using integrating sphere spectrophotometry as described previously [30].

After analysis of characterization data, two finalized formulations were selected to represent fat (F-TMM) and parenchyma tissue (P-TMM). An additional TMM formulation was selected to fabricate imaging targets (T-TMM). To evaluate temporal stability of TMM mass and acoustic properties, three F-TMM and three P-TMM samples were prepared in cell culture flasks and characterized at 1 day and 5 months post-fabrication. All samples were stored at room temperature and pressure. Acoustic characterization samples were weighed at one day and five months to monitor mass loss over time. Average and standard deviation of sample mass and acoustic properties were computed per timepoint, and comparisons between timepoints were made using student's t-test. To study diffusion or leaching of optical additives in embedded PAA-based imaging targets, four two-layer samples were prepared in clear cell culture flasks by forming a bottom layer of transparent control PAA gel (69% w/w DI water, 30% w/w acrylamide/bis solution, 0.2% w/w TEMED, 0.8% APS) and a top layer of the same PAA formulation but including 0.1% w/w of optical absorbers. The first sample contained India ink suspended in a control PAA gel (no additives), the second sample contained India ink suspended in the T-TMM's water phase, the third sample contained water-soluble nigrosin (N4754, Sigma-Aldrich, Inc.) diluted in the T-TMM's water phase, and the fourth sample contained nigrosin suspended in the T-TMM's oil phase. Flasks were photographed every four weeks for five months after fabrication and qualitatively assessed for increased black color in the bottom clear control gel (Supplementary Fig. S1).

2.3. Phantom design and fabrication

A total of five imaging phantoms were fabricated: two preliminary phantoms to test imaging targets prepared with different optical additives (Phantoms 1 and 2), two multi-row phantoms for detailed testing of object detectability (Phantoms 3 and 4), and a one-row phantom for system comparison of boundary buildup artifacts (Phantom 5) (phantom summary in Table 1).

3D modeling software (Fusion 360, Autodesk, San Rafael, CA) was used to design bulk phantom housings as well as two-face injection molds used to fabricate imaging targets. These designs were 3D printed using an affordable LCD 3D printer (Mars 2 Pro, Elegoo, Inc., Shenzhen, China) with 50 μm lateral resolution and 25 μm layer height. Injection molds for cylinder and stepped-cylinder inclusions with diameters ranging from 1 to 4 mm were prepared by inserting a 50.8-μm-diameter stainless steel wire (794600, A-M Systems, Inc., Sequim, WA) through the target mold, which was used to suspend molded targets in empty bulk phantom housings (Fig. 2. A). The two mold faces were then aligned using registration spheres and pressed with a bench vise. T-TMM was injected through a 1 mm opening (Fig. 2. B) using a 25-gauge needle attached to a 3 mL syringe and allowed to cure for approximately

Table 1
Summary of phantom physical characteristics.

		Imaging Targets				
Phantom No.	Background Material	Arrangement	Shape	Dimensions	Material	Depth
1	F-TMM	1 row x 4 columns	Stepped Cylinder	1–4 mm x 5 mm	India Ink in PAA gel	10 mm
2					Nigrosin in T-TMM	
3		4 rows x 4 columns		1–3 mm x 5 mm		10–40 mm
4	P-TMM					
5	F-TMM	1 row x 4 columns	Cylinder	3 mm x 5 mm		10 mm

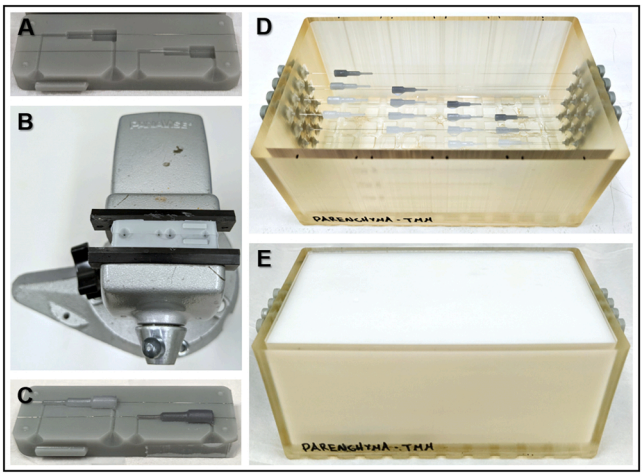

Fig. 2. Assembly of the multi-row phantom (phantoms 3 and 4). A) Two-face target mold with channel for stainless steel wires. B) Two-face mold held in a vise for injection molding. C) Solidified imaging targets in the opened mold. D) Imaging targets suspended in an empty phantom mold in horizontal rows at depths of 10, 20, 30, and 40 mm from the top surface. E) Final imaging phantom after pouring background TMM.

20 min. Finally, molds were disassembled, excess material was removed, and the solid targets were carefully removed (Fig. 2. C).

Phantoms 1 and 2 were fabricated to evaluate the functionality of solid inclusions designed to generate photoacoustic (PA) images containing "filled-in" targets. Here, both phantoms were fabricated containing stepped-cylinder inclusions with diameters of 1, 2, 3, and 4 mm positioned 10 mm deep in a F-TMM background. Phantom 1 contained inclusions prepared with a control PAA gel modified with India ink in DI water, producing μ_a values of 0, 2, 4 and 8 cm^{-1} at 850 nm. Phantom 2 had imaging targets prepared with a T-TMM modified with nigrosin suspended in the oil phase to produce μ_a values of 0.25, 0.5, 1 and 2 cm^{-1} at 850 nm.

In T-TMM, nigrosin is contained in small oil droplets distributed throughout the PAA matrix. However, μ_a was measured in 2-mm thick TMM samples. For targets intended to produce filled-in appearance, two μ_a values need to be considered: 1) the T-TMM's μ_a (as measured) and the estimated droplet μ_a. The μ_a produced from the nigrosin-loaded oil droplets can be estimated as:

$$\mu_{a,droplet} = \frac{\mu_a}{[Oil]} \quad (1)$$

where μ_a is the absorption coefficient measured from a 2-mm slab of TMM [30], and $[Oil]$ is the relative silicone oil concentration by mass in the TMM (12% w/w).

Phantoms 3 and 4 were designed to allow evaluation of multiple aspects of object detectability. A 120 mm (L) x 72 mm (W) x 50 mm (H) phantom housing was 3D printed and prepared containing arrays of stepped-cylinder targets with three 5 mm-long sections with 1, 2 and 3 mm diameters (Supplementary Fig. S2). Rows of four targets horizontally spaced 8 mm apart were positioned at depths of 10, 20, 30 and 40 mm from the phantom's top surface (Fig. 2. D). Each row of targets was spaced 5 mm apart in the phantom's long axis (L) to minimize artifacts such as reflections or optical shadowing, and all targets were at least 20 mm away from the mold walls. Each row contained imaging objects with $\mu_{a,TMM}$ of 0.25, 0.5, 1 and 2 cm^{-1} at 850 nm. Finally, the phantom's background was formed from a 500 g batch of either F-TMM (Phantom 3) or P-TMM (Phantom 4) (recipes summarized in Table 2), which was poured into the phantom housing and allowed to cure for 1 h (Fig. 2. E). After that point, the wires were removed, and the phantoms were kept at room temperature in sealed plastic bags until imaging sessions.

Phantom 5 was prepared to conduct a multi-site phantom-based evaluation of boundary buildup artifacts for three different PAI systems. This phantom was fabricated with straight cylindrical inclusions 3 mm in diameter and 10 mm long positioned at a depth of 10 mm in a F-TMM background. The inclusions were prepared with nigrosin suspended in the oil phase of a T-TMM to produce μ_a values of 0.25, 0.5, 1 and 2 cm^{-1} at 850 nm.

2.4. Phantom imaging and image analysis

PAI systems with different configurations were available to evaluate the functionality of the proposed phantoms. These systems included a custom system located at FDA and two commercial systems at UCSD as described previously [30]. For the custom system, imaging was performed at 850 nm (radiant exposure = 8.2 ± 0.2 mJ/cm^2) with a 10 Hz repetition rate and using either a 7 MHz linear array (L11–4v, Verasonics, Inc., Kirkland, WA) or a 2.5 MHz phased array (P4–1, Philips). Unlike previous studies, transducers were integrated with the 5 mm × 40 mm elliptical optical beam using a custom 3D printed housing (Supplementary Fig. S3). Image reconstruction was performed using Verasonics' proprietary pixel-oriented delay and sum algorithm [55], and images were pulse energy-compensated. The PAI systems available at UCSD included an AcousticX (CYBERDYNE Inc., Japan) and a Vevo LAZR (FUJIFILM VisualSonics, Inc., Ontario, Canada). Both

Table 2
Formulation to form 100 g of control PAA gel, F-TMM, P-TMM, and T- TMM. Values shown as (%) represent concentration of previously prepared/purchased stock solutions.

	Control PAA	Fat TMM	Parenchyma TMM	Target TMM
DI Water	69 g	56.48 g	41.59 g	46.88 g
TiO_2 Suspension (2.5% w/w)	–	0.4 g	3.2 g	–
Ethylene Glycol	–	–	17.25 g	–
Silicone Oil - 100 cSt	–	12 g	–	12 g
Silicone Oil - 350 cSt	–	–	0.65 g	–
Silicone Oil - 1000 cSt	–	–	6.25 g	–
Tween 20	–	0.12 g	0.06 g	0.12 g
Acrylamide/Bis (40% w/v)	30 g	30 g	30 g	30 g
Carbomer 940 (0.2% w/w)	–	–	–	10 g
TEMED	0.2 g	0.2 g	0.2 g	0.2 g
APS Solution (10% w/w)	0.8 g	0.8 g	0.8 g	0.8 g

systems have been previously described and fully characterized [30]. Imaging with the AcousticX was performed using 850 nm LED arrays (radiant exposure = 0.028 mJ/cm^2) at a 4 kHz repetition rate and a 10 MHz linear array transducer, while the Vevo LAZR was tuned to 850 nm (radiant exposure = 8.6 ± 0.3 mJ/cm^2) at a 20 Hz repetition rate and used a 15 MHz transducer (LZ201).

For the multi-site evaluation, Phantom 5 was constructed at FDA, weighed, and imaged with the custom PAI system. After imaging, the phantom was placed in a sealed plastic bag, packed in a cardboard box, and mailed to UCSD using 2-day express shipping. On arrival, the phantom was weighed to check for mass loss during shipment, and then imaged using the AcousticX and Vevo LAZR systems.

A set of imaging guidelines was developed to standardize data collection across PAI systems. First, transducers were coupled to the phantom using ultrasound gel and aligned such that were normal to the imaging targets, capturing each row of inclusions in a single field of view (FOV). Imaging was performed at 850 nm with maximum output energy for each system. Preprocessed photoacoustic images (linear amplitude images) were acquired at five locations along the cylindrical targets' long axes. Image reconstruction was performed using built-in algorithms setting the reconstruction speed of sound to match the background TMM's properties. Image quality metrics were computed on non-compressed, linear amplitude images.

To evaluate object detectability, square regions of interest (ROI) were drawn over each target in addition to equal-sized, local background ROIs drawn to the left of each inclusion. ROI dimensions were set to 0.5 mm larger than specific target diameter (e.g., 2 mm target ROIs were 2.5 mm × 2.5 mm). Signal-to-background ratio (SBR) was calculated for each target as:

$$SBR = \frac{A_t}{A_b} \tag{2}$$

where A_t is the average target ROI amplitude and A_b is the average background ROI amplitude [30].

To assess boundary buildup, ROIs were drawn at the target's top boundary. Boundary ROI was set to 0.5 mm larger than specific target width and half of target height (e.g., boundary ROIs for 2 mm targets were 2.5 mm × 1 mm). Similarly, square ROIs with sides equal to half of the target's diameter were drawn over the core of each target (e.g., core ROIs for 3 mm targets were 1.5 ×1.5 mm). Boundary buildup was evaluated as:

$$Boundary\ Buildup = \frac{A_{core}}{A_{boundary}} \tag{3}$$

where A_{core} is the average core ROI amplitude and $A_{boundary}$ is the average boundary ROI amplitude.

Geometric accuracy was evaluated by analysis of log-compressed PA images. The outer edges of imaging targets were identified by inspection and both horizontal and vertical distances between edges were measured using software-based calipers. Spatial measurement error for target diameter (e_D) was calculated in both directions as:

$$e_D = 100\% \times |D_{actual} - D_{measured}|/D_{actual} \tag{4}$$

where D_{actual} is the nominal target dimension and $D_{measured}$ is the PAI-derived measurement [56].

3. Results

3.1. TMM properties

Tunability of the TMM's acoustic properties is summarized in Fig. 3. While α increased with silicone oil concentration, c_s was inversely affected. Acoustic attenuation was linear with both oil concentration up to 27.6% w/w (R^2 >0.92) for a 100 cSt oil, and with oil viscosity from 50 to 350 cSt (R^2 >0.99) at a fixed concentration of 13.8% w/w. Speed of sound decreased linearly from 1475 to 1314.5 m/s with increasing silicone oil concentration from 6% to 27.6% w/w (R^2 >0.98). Increase of emulsification parameters such as intensity and time decreased α, but not c_s. Increasing ethylene glycol concentration from 6.9% to 17.25% w/

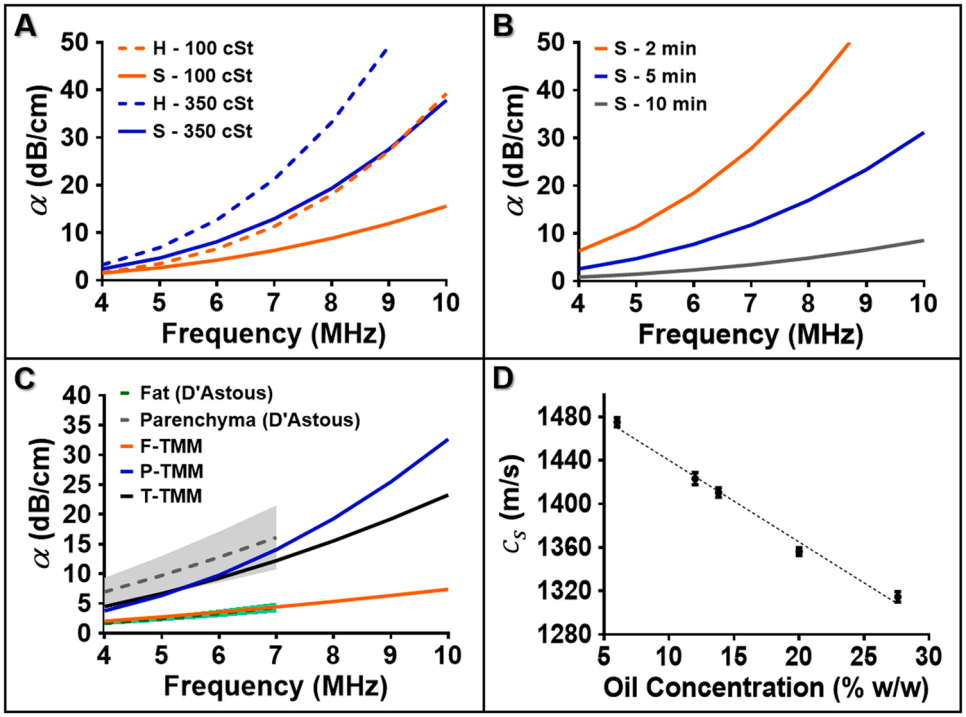

Fig. 3. TMM acoustic properties. A) α vs. frequency, oil viscosity and emulsification method (H = homogenizer, S = probe sonicator). B) α vs. frequency and sonication duration for a TMM prepared with 1000 cSt silicone oil emulsified with a probe sonicator at 100% amplitude. C) α of the final phantom TMMs compared to literature values for ex vivo human breast tissue [31]. D) c_s vs. concentration of 100 cSt silicone oil sonicated at 60% amplitude for 2 min.

w increased c_s from 1498 to 1572 m/s, but α was not significantly altered. These results show that c_s can be readily tuned by varying silicone oil and ethylene glycol concentrations, and α can be tuned by varying oil viscosity and emulsification parameters.

As expected, TMM optical properties were highly tunable and showed high linearity with respect to additive concentration (Fig. 4). Both PAA samples containing India ink and nigrosin showed highly linear increases in μ_a vs. additive concentration, and μ_a values at 850 nm from 0.25 to 8 cm^{-1} were achieved. The μ_s' was highly linear vs. TiO_2 concentration over the range tested (R^2 >0.99). Based on characterization results, F-TMM, P-TMM, and T-TMM formulations were selected for phantom fabrication (Table 3).

TMM samples showed good resistance to desiccation, with mass loss over five months of 1.2% and 1.9% for F-TMM and P-TMM, respectively. After five months, c_s decreased by 4 ± 0.9 m/s (0.28% ± 0.063%) and 14 ± 4.5 m/s (0.89% ± 0.287%), for F-TMM and P-TMMs respectively. α at 7 MHz decreased over 5 months by 0.18 ± 0.16 dB/cm (4.16 ± 3.63%) and 2.64 ± 0.16 dB/cm (6.15 ± 4.56%) for F-TMM and P-TMM, respectively. These variations are within 10% of baseline, the acoustic property tolerance recommended by the ultrasound standard IEC 61391–1:2017 [57]. Qualitative evaluation of optical additive stability by photography over a period of 5 months indicated no significant observed diffusion of nigrosin embedded in silicone oil droplets into adjacent control PAA gel (Supplementary Fig. S1). Similarly, suspension of India ink in either a PAA gel or the TMM's water phase showed high stability. However, a PAA gel sample modified with water-soluble nigrosin showed rapid diffusion of the dye throughout the control PAA hydrogel.

3.2. Image quality evaluation

Imaging results in preliminary phantoms (phantoms 1 and 2) are shown in Fig. 5. The deposition of optical absorbers in either a homogeneous PAA hydrogel (India ink), or in discrete oil droplets in the T-TMM (nigrosin) led to different PA signal patterns. Targets containing India ink resulted in a lack of lumen signals and presence of bright top/bottom boundary signals, while nigrosin-in-oil targets produced PA image features with a more filled-in appearance. The nigrosin-in-oil target approach was selected for further use in imaging phantoms.

Table 3
Acoustic and optical properties of final Fat, Parenchyma and Target TMMs.

	F-TMM	P-TMM	T-TMM
α (7 MHz)	4.41 dB/cm	14.07 dB/cm	12.21 dB/cm
c_s	1423 m/s	1536 m/s	1424 m/s
μ_a (850 nm)	0.09 cm^{-1}	0.11 cm^{-1}	0.25 – 2 cm^{-1}
μ_s' (850 nm)	7.02 cm^{-1}	11.72 cm^{-1}	5.75 cm^{-1}

Several artifacts were present in the images (Figs. 5 and 6). The custom system produced near-field clutter due to optical absorption at the transducer/phantom interface. Similarly, reflection artifacts can be observed under the imaging targets. Both artifacts are likely due to photoacoustic signals generated at the transducer surface traveling downward and reflecting off the phantom surface or targets, which doubles the time of flight and the resulting depth determined by image reconstruction. To reduce near-field clutter, transducers were gel-coupled with aluminum foil. The foil reduces light absorption at the transducer face, which generates unwanted photoacoustic image clutter. However, the attachment of the foil to the transducer is challenging, and x-shaped artifacts can be generated by warps or imperfections in the foil (Fig. 5).

Representative ultrasound and PA images of the F-TMM multi-row phantom are shown in Fig. 6. Clear differences in target appearance and detectability were observed in PA images, as a function of target properties and the background TMM. For instance, four imaging objects can be easily observed at depths of 10 mm and 20 mm, while only the top and bottom surface of some of the objects can be distinguished at 30 mm depth. Some targets are not detectable due to tissue-like optical

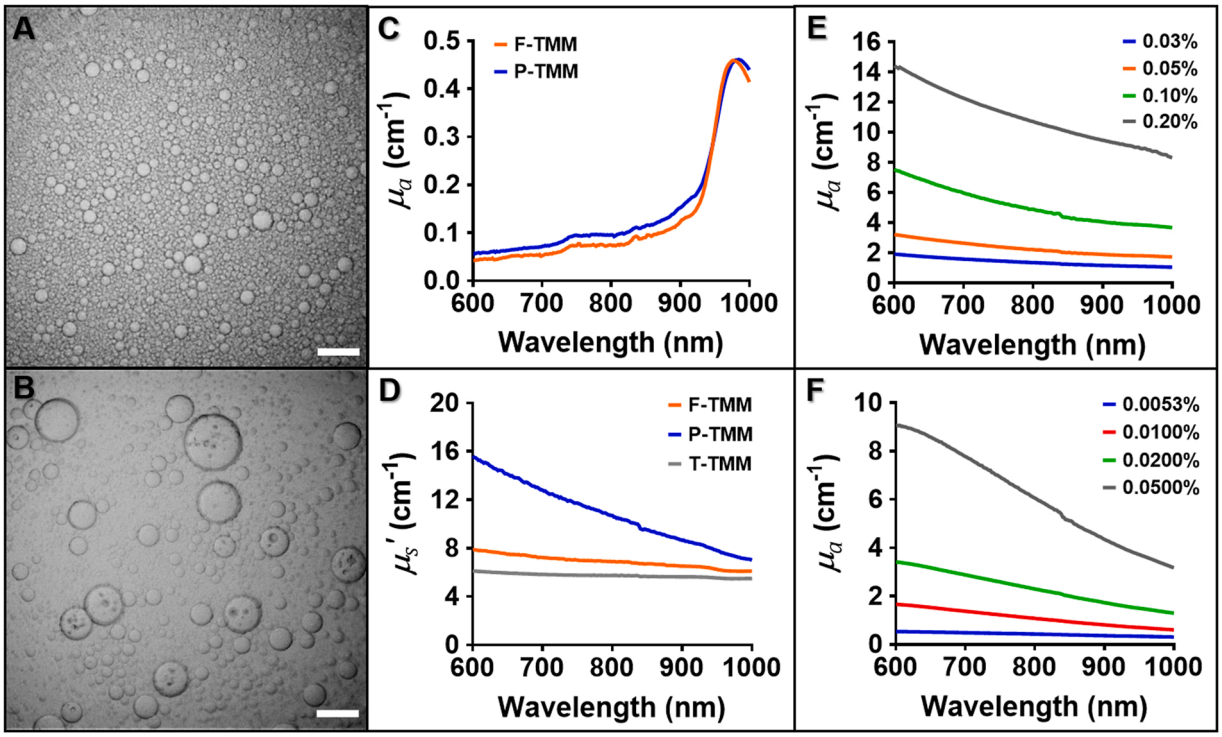

Fig. 4. TMM optical properties. Bright field microscopy of A) F-TMM and B) P-TMM samples. Scale bars = 50 μm. C) μ_a and D) μ_s' spectra of F-TMM, P-TMM, and T-TMM samples. E) μ_a of India ink suspended in the control PAA gel. F) μ_a of alcohol-soluble nigrosin suspended in the oil phase of T-TMM. Concentrations are expressed as % w/w of total TMM mass.

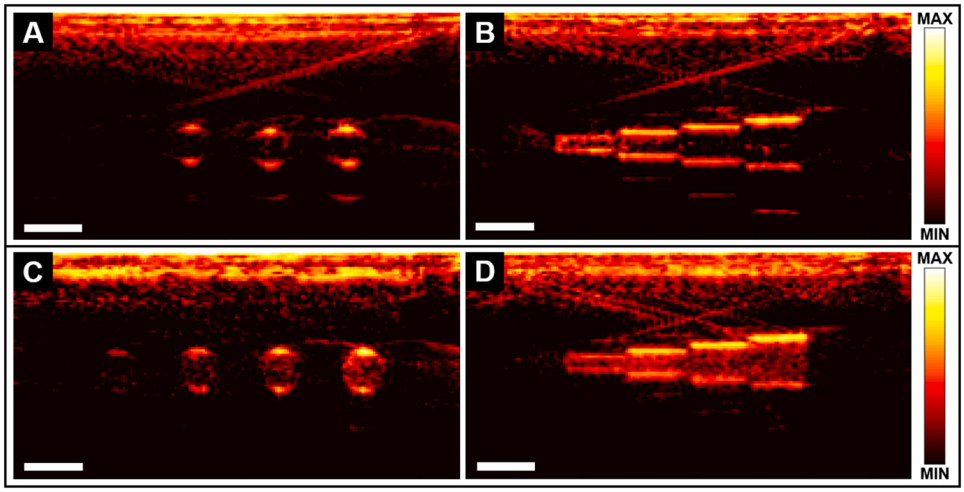

Fig. 5. PA images of stepped-cylinder inclusions producing either boundary buildup or filled-in object appearance in preliminary phantoms (phantoms 1 and 2). Left column (A and C) shows cross sections of 3 mm diameter sections. Right column (B and D) shows side views of imaging targets with sections of 1, 2, 3 and 4 mm diameter. A-B) India ink-in-hydrogel T-T-TMM targets. C-D) Nigrosin-in-oil T-TMM targets. μ_a values from left to right: A) 0, 2, 4 and 8 cm^{-1} at 850 nm and B) 0.25, 0.5, 1 and 2 cm^{-1} at 850 nm (C). Scale bars = 5 mm. Display dynamic range: 32 dB. Images acquired using the L11–4 transducer.

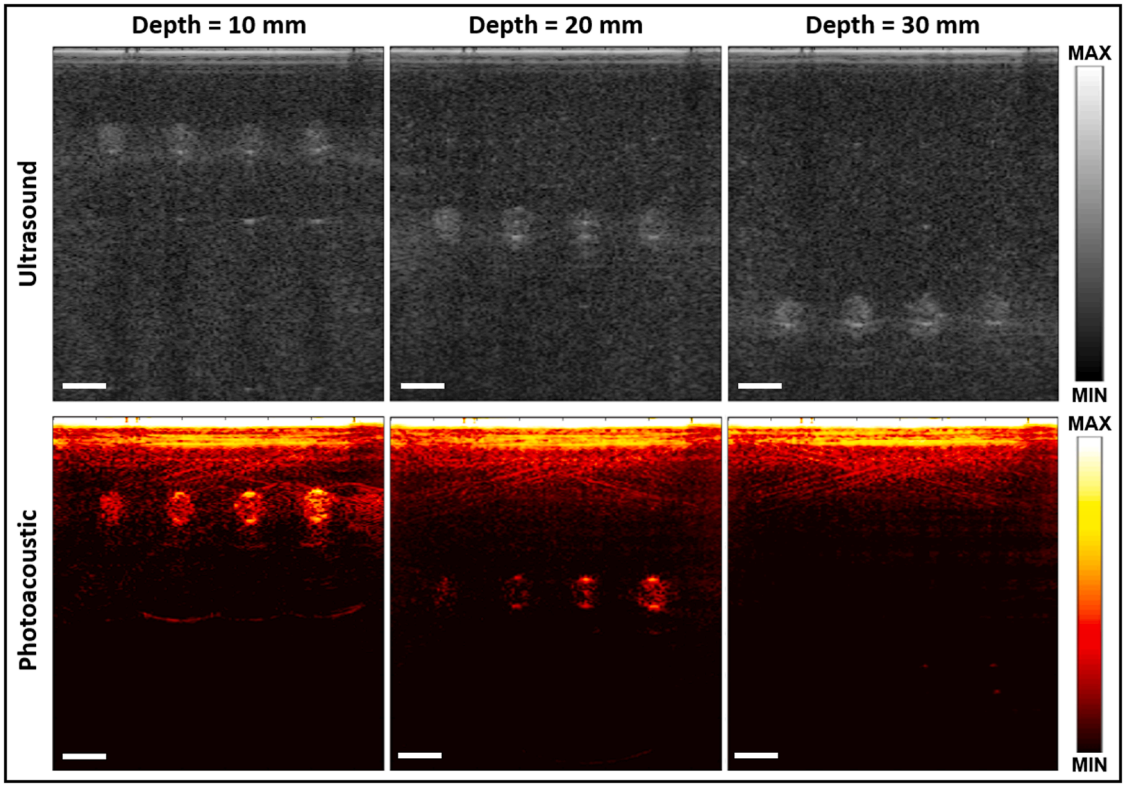

Fig. 6. Representative ultrasound (top row) and PA images (bottom row) of Phantom 3 using the custom system with the L11–4v transducer, showing 3 mm diameter target segments embedded in F-TMM at depths of 10 mm, 20 mm, and 30 mm (40 mm targets not shown). μ_a values from left to right: 0.25, 0.5, 1 and 2 cm^{-1} at 850 nm. Scale bars = 5 mm. Display dynamic range: US = 45 dB, PA = 38 dB.

and acoustic attenuation in the phantom, which is a desirable effect for phantom-based image quality testing. By ensuring at least one target in a series is present but undetectable by an instrument, the limits of detection can be bounded and thus interpolated, rather than relying on extrapolation to determine such limits.

As expected, maximum imaging depth was closely related to target μ_a. Targets with μ_a values ≥ 1 cm^{-1} were visually detectable at maximum depths of 30 mm in F-TMM and 10 mm in P-TMM (Fig. 7). This difference may be attributed to higher acoustic attenuation in P-TMM phantoms. However, size-dependent detectability was also observed. PA amplitude and SBR values were highly linear and comparable across objects of same μ_a with different diameters (Fig. 8). For targets embedded in F-TMM, SBR values greater than 1 indicated detectable objects. However, the 1 mm target with μ_a of 0.25 cm^{-1} at 20 mm depth in F-TMM resulted in a SBR of 0.95 ± 0.04 and was not visually detectable, while larger targets (2 and 3 mm) with same μ_a showed higher SBR values (1.07 ± 0.02 and 1.11 ± 0.01, respectively) and were still observable. Core/boundary ratio generally decreased with increasing target μ_a. However, selection of core ROIs for 1 mm targets was not possible due to the close proximity of the two boundaries.

Several trends were identified from geometric accuracy analysis. Diameter measurement error generally increased with target μ_a, decreased with depth, and was decreased with target size (Table 4). For example, spatial measurements of 3-mm targets in F-TMM at 10 mm

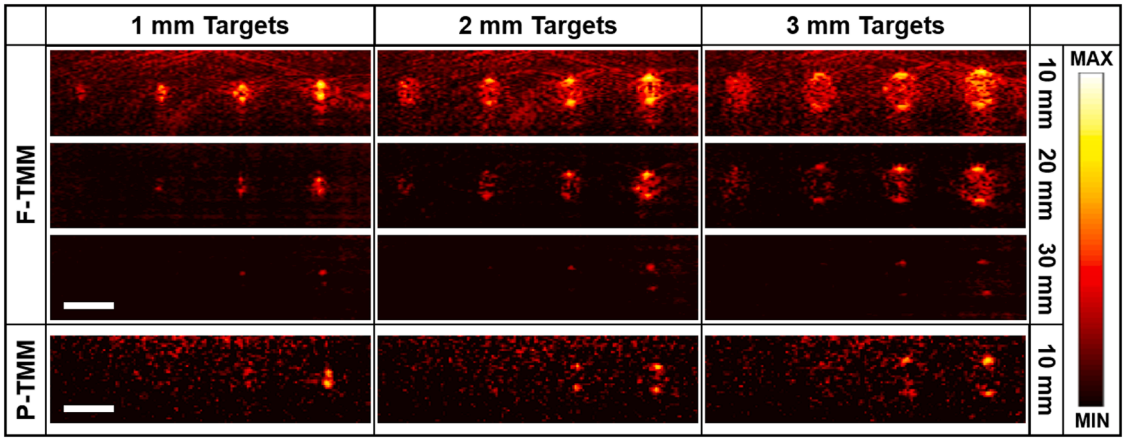

Fig. 7. Log-compressed PA images of multi-row phantoms (phantoms 3 and 4) with 1–3 mm targets with μ_a values of 0.25, 0.5, 1 and 2 cm^{-1} (left to right in each image) embedded in fat (F-TMM) or parenchyma (P-TMM) backgrounds at depths of 10 mm, 20 mm, 30 mm and 40 mm (40 mm not shown). Images acquired using the custom system with the L11–4 transducer. Scale bars = 5 mm. Display dynamic range: F-TMM (38 dB) and P-TMM (26 dB).

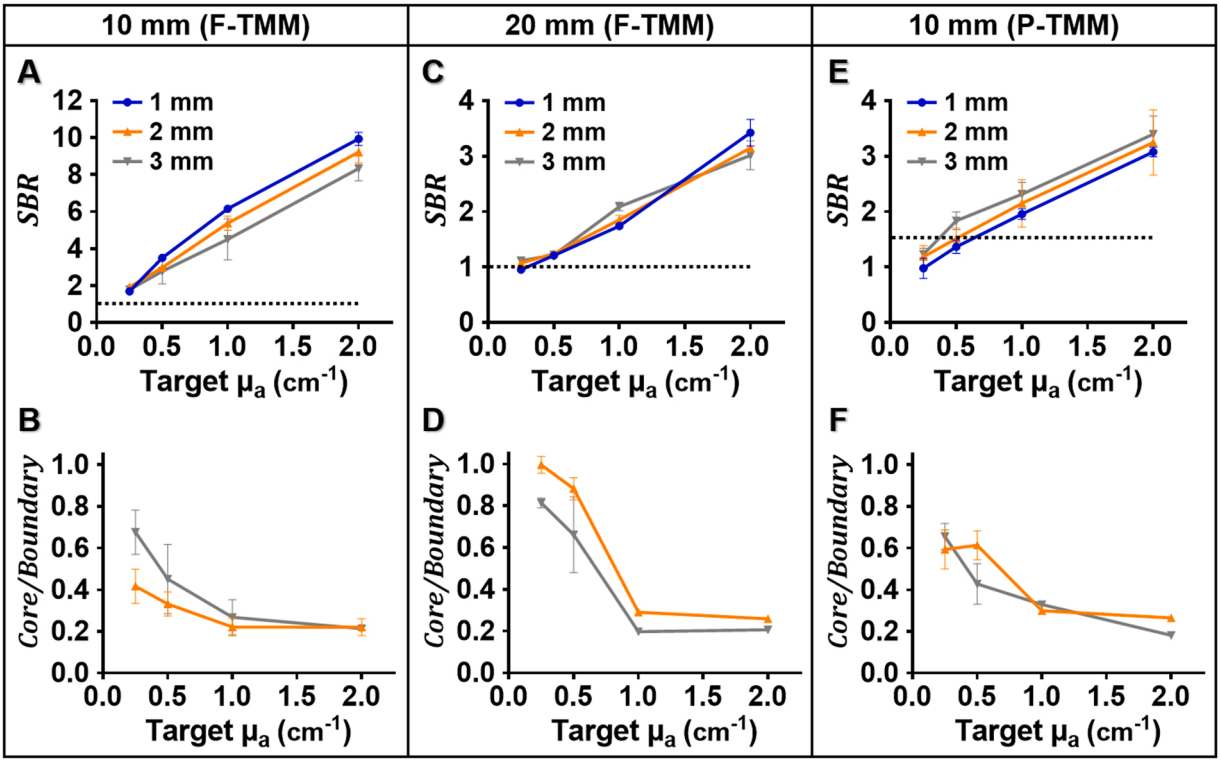

Fig. 8. Quantitative image quality evaluation from PA images of phantoms 3 and 4. A) SBR and B) Core/Boundary ratio of targets embedded in F-TMM at 10 mm depth. C) SBR and D) Core/Boundary ratio of targets embedded in F-TMM at 20 mm depth. E) SBR and F) Core/Boundary ratio of targets embedded in P-TMM at 10 mm depth. Dashed lines represent detectability based on SBR values that match visual inspection of PA images.

Table 4
Vertical spatial measurement error (e_D) vs. target diameter, μ_a, depth, and background TMM using the L11–4 transducer.

		1 mm Target				2 mm Target				3 mm Target			
	μ_a (cm^{-1})	0.25	0.5	1	2	0.25	0.5	1	2	0.25	0.5	1	2
F-TMM	10 mm	22.8	55.5	77.5	85.9	6.3	22.8	31.7	42.6	10.1	22.8	26.7	30.7
	20 mm	–	21.2	45.9	51.2	21.7	13.6	18.6	25.4	2.6	11.2	18.1	20.9
	30 mm	–	–	10.8	22.3	–	–	8.4	14.7	–	–	7.6	8.8
P-TMM	10 mm	–	–	51.9	47.2	–	–	16.6	12.2	–	–	10.1	18.6

depth resulted in z-axis e_D of 10.1% and 30.7% for targets with μ_a values of 0.25 and 2 cm^{-1}, respectively. Measurement errors of 1-mm targets under same conditions, resulted in 22.8% and 85.9%, respectively. Diameter of high contrast objects was generally overestimated by PAI. However, the dimensions of objects with low μ_a (≤ 0.5 cm^{-1}) positioned at depths > 10 mm were often underestimated (e.g., 2-mm target with $\mu_a = 0.25$ cm^{-1} at 20 mm depth in F-TMM).

Analysis of images acquired in the straight cylinder phantom (Phantom 5) showed linear response of SBR to target μ_a on all three systems (Fig. 9). However, sensitivity decreased with increasing transducer center frequency. For instance, the VevoLAZR (15 MHz) showed the poorest sensitivity, barely detecting the target with $\mu_a = 0.5$ cm^{-1}. In contrast, the custom system using the P4–1 transducer (2.5 MHz) detected all targets down to $\mu_a = 0.25$ cm^{-1}. Core/boundary ratio increased with increasing transducer center frequency and slightly decreased with increasing target μ_a. Diameter measurement error decreased with transducer center frequency.

4. Discussion

In this study, we developed and characterized an emulsion-based hydrogel TMM offering broad tunability of optical and acoustic properties. Solid stepped-cylinder targets were fabricated with different diameters and μ_a, then embedded in imaging phantoms to enable evaluation of several aspects of object detectability. These phantoms had good temporal stability and were sufficiently robust for shipment across the United States for a multi-site imaging test.

The addition of emulsified silicone oil to PAA hydrogels affected both c_s and α. Variations in oil properties (concentration, viscosity) and emulsification parameters (amplitude, duration) led to significant changes in TMM properties, and this effect should be carefully considered and controlled during fabrication of such materials. c_s decreased linearly with increasing silicone oil concentration (down to 1314 m/s) and increased with ethylene glycol (up to 1572 m/s). Addition of ethylene glycol did not cause significant changes in α, perhaps due to its better miscibility in water than silicone oil. In general, TMMs with bigger oil droplets produced higher α values. We reduced acoustic attenuation to biologically relevant ranges by using oils with lower viscosities, increasing emulsification intensity, and/or increasing emulsification duration. These results indicate a significant improvement in acoustic tunability compared to our previous PAA formulation [30], without significantly increasing material cost or preparation time. For instance, a multi-row phantom (phantoms 3 and 4) can be assembled in approximately 10 h including 3D-printing time, TMM preparation and phantom assembly.

TMM characterization samples were stable for at least five months, which is consistent with the reported service life of several years for Zerdine® (CIRS, Inc., Norfolk, VA), a commercially available ultrasound TMM based in PAA [53]. Minor changes on acoustic properties could be explained by the desiccation typical of hydrogels. The greater changes seen in P-TMM vs. F-TMM may be due to the higher water content of P-TMM (62.7% w/w vs. 57.6% w/w). Larger imaging phantoms were

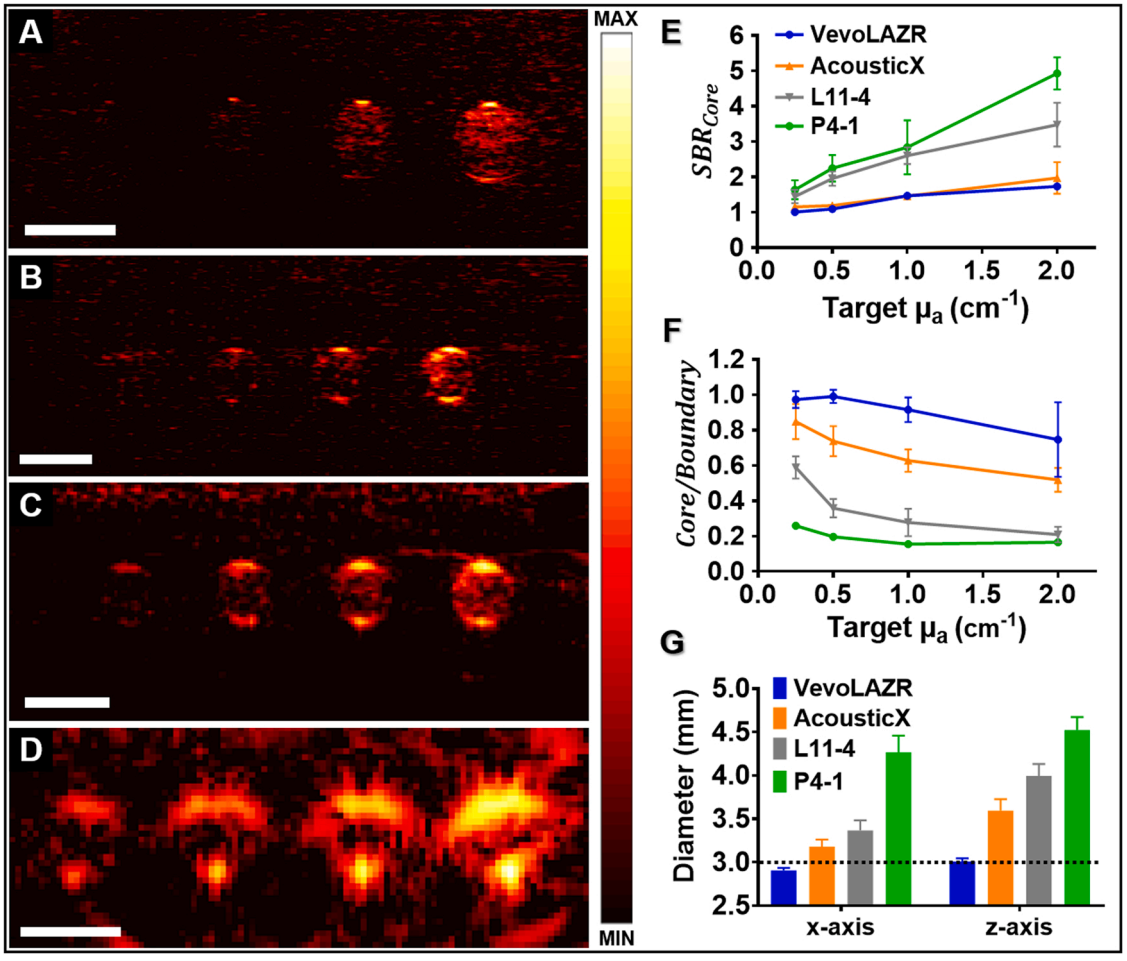

Fig. 9. Multi-system analysis of the straight cylinder phantom (Phantom 5). Log-compressed PA images acquired with the A) VevoLAZR, B) AcousticX, and custom system with C) L11–4 and D) P4–1 transducers. E) Core SBR vs. μ_a for each imaging system. F) Core/boundary ratio vs. μ_a and imaging system. G) Diameter measurements from each PAI system (for target with $\mu_a = 2$ cm^{-1}). Dashed line represents nominal target diameter. Scale bars = 5 mm. Display dynamic ranges: Vevo LAZR (20 dB), AcousticX (20 dB), L11–4 (32 dB), P4–1 (34 dB).

also temporally stable over eight weeks (~1% mass loss), despite undergoing cross-country transport and having one surface exposed to air during imaging experiments. While phantoms were stored in sealed plastic bags outside of use, in future work we will design optimized housings and storage practices, including addition of a thin plastic membrane over the imaging surface ("acoustic window") to reduce desiccation. This approach is commonly used in commercial imaging phantoms [58]. Photography of heterogeneous two-layer samples indicated that as expected, suspensions of India ink particles in the TMM's water phase did not undergo diffusion/leaching. Interestingly, nigrosin suspended in the TMM's oil phase also did not diffuse into adjacent TMM regions. These approaches are suitable for fabricating stable solid inclusions embedded in TMM as imaging targets.

3D printing facilitated fabrication of solid PAA inclusions with tunable properties that could be embedded in background PAA TMM. Solid inclusions offer advantages over the traditional approach of using embedded tubes filled with absorptive dyes [40], including: 1) solid inclusions can be molded into irregular shapes with variable dimensions, 2) there is no need to inject solutions, design external connections and fittings, or clean fluid channels after use, and 3) the optical and acoustic property mismatch at target interface with background TMM is better controlled. Additionally, while targets containing India ink suspended in the water phase produced strong boundary buildup artifacts usually encountered in phantom testing [43,59], targets that used nigrosin dissolved in TMM oil phase yielded PA image features with a more filled-in appearance. This was expected as PAI should be able to detect signals from several small, point-like absorbers, although this effect may also have been caused by acoustic scattering by the suspended droplets. This is supported by the positive ultrasound contrast of phantom targets and high relative volume fraction of droplets (estimated at ~12% based on concentration). It is also possible that some of the core signal in PA images was caused by out-of-plane artifact from sources outside of the image plane. Nevertheless, image quality analysis indicated that the core region amplitude was still linear with target μ_a. This implies that these core signals are proportional to absorption coefficient and would thus be suitable for evaluating performance of quantitative and/or spectroscopic PAI methods such as oximetry. Several studies have shown that PA images of large tissue regions present distributed signal throughout the field of view, which may be due to dense groups of small, even sub-resolution vessels [1,60,61]. While traditional homogeneous absorptive targets or fluid channels are useful for representing large blood vessels, these novel filled-in targets may be useful as idealized mimics for ensembles of small, sub-resolution photoacoustic sources including microvasculature [62] or deposits of contrast agents like nanoparticles [63].

Although the range of bulk μ_a values selected for phantom targets appears lower than values expected for blood, the estimated $\mu_{a,droplet}$ varied from 2 to 16 cm^{-1}, which overlaps with the biologically relevant range of ~2–6 cm^{-1} for 850 nm. For instance, a $\mu_{a,droplet}$ of 5.3 cm^{-1} at 850 nm would correspond to a normal total hemoglobin concentration of 14 g/dL at 100% SO_2 [64–66]. Similarly, a $\mu_{a,droplet}$ of 2.6 cm^{-1} at 850 nm would represent a low-contrast scenario, such as anemia with total hemoglobin concentration of ~7 g/dl at 100% SO_2. Targets prepared with bulk μ_a values outside of this range (0.25–2 cm^{-1}) showed a decrease in linearity due to either weak signal (< 0.25 cm^{-1}) or saturation effects (> 2 cm^{-1}).

Evaluation of the multi-row phantom indicated size-dependent object detectability, especially for targets with $\mu_a = 0.25$ cm^{-1}. In general, larger targets (2–3 mm diameter) were more easily detectable at low μ_a and greater depth in the F-TMM phantom. Target boundary signals were generally detected to depths of 20–30 mm with the L11–4v transducer depending on target μ_a, and this is consistent with previous studies using breast-mimicking plastisol phantoms with tube targets at μ_a of 4/cm^{-1} at 800 nm [43]. Interestingly, if object detectability had been defined based on core signal alone, reported imaging depths would be substantially worse due to lower core signal vs. depth. Imaging depth was much more limited in P-TMM, with even the highest absorbing target only being detected at 10 mm depths. This may be attributed to the higher acoustic attenuation of P-TMM vs. F-TMM (14 dB/cm vs. 4.4 dB/cm at 7 MHz). However, the P4–1 phased array (2.5 MHz) was capable of detecting targets down to 40 mm in both F-TMM and P-TMM phantoms (Supplementary Fig. S4). It is notable that many PAI systems intended for breast imaging use transducers with lower center frequencies, although this typically reduces spatial resolution performance [8]. It was notable that targets which were readily detected by visual inspection yielded SBR values close to 1, where SBR = 1 would normally describe a completely undetectable object (target and background having equal amplitude). ROI measurements in this study may have been generally lower as we did not use a binary mask to finely trim adjacent background or weak pixels from ROI selections as in previous studies [43]. These weak pixels could have lowered average target ROI amplitudes and thus yielded lower SBR values. We found that such masks were not well-suited to selecting target core signals unless carefully tuned to each target, which represents a more burdensome approach.

Phantom testing of three PAI systems indicated a performance tradeoff between sensitivity and geometric accuracy. While sensitivity decreased with increasing transducer center frequency (Fig. 9. E), objects appeared more homogeneous, with stronger core signal leading to core/boundary ratios approaching 1. Observed variations in geometric accuracy across different systems could be explained by multiple mechanisms. First, boundary buildup was more evident in transducers with low center frequency, which may be due to lower spatial resolution blurring target edge features and preventing visualization of absorbing droplets. The lower acoustic scattering at lower frequencies may also have contributed to reduced core signal amplitudes for lower frequency transducers. Third, targets (especially edge features) may have undergone vertical broadening due to out-of-plane signal contributions, which travel greater pathlengths and are thus reconstructed underneath the in-plane feature [43].

5. Conclusion

In conclusion, we developed stable, tunable emulsion hydrogel phantoms containing solid hydrogel inclusions with controllable diameter, depth, and properties. Embedded inclusions achieved less boundary buildup and a more filled-in target appearance, which may be useful for characterizing size-dependent object detectability in terms of sensitivity, imaging depth, geometric accuracy, and boundary buildup artifacts. Phantom production was made simple, fast, and inexpensive through use of 3D printing, which can also improve repeatability and facilitate fabrication and use of these tools by others. These phantoms and test methods may support advancements in PAI device design optimization and aid development of standardized PAI test methods that will ultimately accelerate clinical translation of PAI technology.

Funding source

We gratefully acknowledge funding from the NSF/FDA Scholar-in-Residence program (Awards #1842387, #1937674, and #2149602). JVJ also acknowledges infrastructure from NIH under grants S10 OD023555 and S10 OD021821.

Declaration of Competing Interest

The authors declare that no conflicts of interest exist.

Disclaimer

The mention of commercial products, their sources, or their use in connection with material reported herein is not to be construed as either

an actual or implied endorsement of such products by the Department of Health and Human Services. This article reflects the views of the authors and should not be construed to represent FDA's views or policies.

Appendix A. Supporting information

Supplementary data associated with this article can be found in the online version at doi:10.1016/j.pacs.2022.100348.

References

[1] E.I. Neuschler, R. Butler, C.A. Young, L.D. Barke, M.L. Bertrand, M. Bohm-Velez, S. Destounis, P. Donlan, S.R. Grobmyer, J. Katzen, K.A. Kist, P.T. Lavin, E. V. Makariou, T.M. Parris, K.J. Schilling, F.L. Tucker, B.E. Dogan, A pivotal study of optoacoustic imaging to diagnose benign and malignant breast masses: a new evaluation tool for radiologists, Radiology 287 (2) (2018) 398–412.

[2] S. Manohar, M. Dantuma, Current and future trends in photoacoustic breast imaging, Photoacoustics 16 (2019), 100134.

[3] S. Gargiulo, S. Albanese, M. Mancini, State-of-the-art preclinical photoacoustic imaging in oncology: recent advances in cancer theranostics, Contrast Media Mol. Imaging 2019 (2019), 5080267.

[4] J. Su, A. Karpiouk, B. Wang, S. Emelianov, Photoacoustic imaging of clinical metal needles in tissue, J. Biomed. Opt. 15 (2) (2010), 021309.

[5] J. Jo, G. Xu, M. Cao, A. Marquardt, S. Francis, G. Gandikota, X. Wang, A functional study of human inflammatory arthritis using photoacoustic imaging, Sci. Rep. 7 (1) (2017) 15026.

[6] L.V. Wang, S. Hu, Photoacoustic tomography: in vivo imaging from organelles to organs, Science 335 (6075) (2012) 1458–1462.

[7] A.A. Oraevsky, B. Clingman, J. Zalev, A.T. Stavros, W.T. Yang, J.R. Parikh, Clinical optoacoustic imaging combined with ultrasound for coregistered functional and anatomical mapping of breast tumors, Photoacoustics 12 (2018) 30–45.

[8] N. Nyayapathi, J. Xia, Photoacoustic imaging of breast cancer: a mini review of system design and image features, J. Biomed. Opt. 24 (12) (2019) 1–13.

[9] S.L. Vieira, T.Z. Pavan, J.E. Junior, A.A. Carneiro, Paraffin-gel tissue-mimicking material for ultrasound-guided needle biopsy phantom, Ultrasound Med Biol. 39 (12) (2013) 2477–2484.

[10] E. Maneas, W. Xia, O. Ogunlade, M. Fonseca, D.I. Nikitichev, A.L. David, S.J. West, S. Ourselin, J.C. Hebden, T. Vercauteren, A.E. Desjardins, Gel wax-based tissue-mimicking phantoms for multispectral photoacoustic imaging, Biomed. Opt. Express 9 (3) (2018) 1151–1163.

[11] E. Zhang, J. Laufer, P. Beard, Backward-mode multiwavelength photoacoustic scanner using a planar Fabry-Perot polymer film ultrasound sensor for high-resolution three-dimensional imaging of biological tissues, Appl. Opt. 47 (4) (2008) 561–577.

[12] F. Ratto, L. Cavigli, C. Borri, S. Centi, G. Magni, M. Mazzoni, R. Pini, Hybrid organosilicon/polyol phantom for photoacoustic imaging, Biomed. Opt. Express 10 (8) (2019) 3719–3730.

[13] S.E. Bohndiek, S. Bodapati, D. Van De Sompel, S.R. Kothapalli, S.S. Gambhir, Development and application of stable phantoms for the evaluation of photoacoustic imaging instruments, PLoS One 8 (9) (2013), e75533.

[14] G.M. Spirou, A.A. Oraevsky, I.A. Vitkin, W.M. Whelan, Optical and acoustic properties at 1064 nm of polyvinyl chloride-plastisol for use as a tissue phantom in biomedical optoacoustics, Phys. Med. Biol. 50 (14) (2005) N141–N153.

[15] W.C. Vogt, C. Jia, K.A. Wear, B.S. Garra, T. Joshua Pfefer, Biologically relevant photoacoustic imaging phantoms with tunable optical and acoustic properties, J. Biomed. Opt. 21 (10) (2016), 101405.

[16] M. Dantuma, R. van Dommelen, S. Manohar, Semi-anthropomorphic photoacoustic breast phantom, Biomed. Opt. Express 10 (11) (2019) 5921–5939.

[17] L.C. Cabrelli, F.W. Grillo, D.R.T. Sampaio, A.A.O. Carneiro, T.Z. Pavan, Acoustic and elastic properties of glycerol in oil-based gel phantoms, Ultrasound Med Biol. 43 (9) (2017) 2086–2094.

[18] L.C. Cabrelli, J.H. Uliana, L.B. da Cruz Junior, L. Bachmann, A.A.O. Carneiro, T. Z. Pavan, Glycerol-in-SEBS gel as a material to manufacture stable wall-less vascular phantom for ultrasound and photoacoustic imaging, Biomed. Phys. Eng. Express 7 (6) (2021).

[19] J.R. Cook, R.R. Bouchard, S.Y. Emelianov, Tissue-mimicking phantoms for photoacoustic and ultrasonic imaging, Biomed. Opt. Express 2 (11) (2011) 3193–3206.

[20] Y.S. Chen, W. Frey, S. Kim, P. Kruizinga, K. Homan, S. Emelianov, Silica-coated gold nanorods as photoacoustic signal nanoamplifiers, Nano Lett. 11 (2) (2011) 348–354.

[21] A.B. Karpiouk, S.R. Aglyamov, S. Mallidi, J. Shah, W.G. Scott, J.M. Rubin, S. Y. Emelianov, Combined ultrasound and photoacoustic imaging to detect and stage deep vein thrombosis: phantom and ex vivo studies, J. Biomed. Opt. 13 (5) (2008), 054061.

[22] L. Ding, X. Luis Dean-Ben, C. Lutzweiler, D. Razansky, V. Ntziachristos, Efficient non-negative constrained model-based inversion in optoacoustic tomography, Phys. Med. Biol. 60 (17) (2015) 6733–6750.

[23] C. Avigo, N. Di Lascio, P. Armanetti, C. Kusmic, L. Cavigli, F. Ratto, S. Meucci, C. Masciullo, M. Cecchini, R. Pini, F. Faita, L. Menichetti, Organosilicon phantom for photoacoustic imaging, J. Biomed. Opt. 20 (4) (2015) 46008.

[24] J. Levi, S.R. Kothapalli, S. Bohndiek, J.K. Yoon, A. Dragulescu-Andrasi, C. Nielsen, A. Tisma, S. Bodapati, G. Gowrishankar, X. Yan, C. Chan, D. Starcevic, S. S. Gambhir, Molecular photoacoustic imaging of follicular thyroid carcinoma, Clin. Cancer Res. 19 (6) (2013) 1494–1502.

[25] G. Kim, S.W. Huang, K.C. Day, M. O'Donnell, R.R. Agayan, M.A. Day, R. Kopelman, S. Ashkenazi, Indocyanine-green-embedded PEBBLEs as a contrast agent for photoacoustic imaging, J. Biomed. Opt. 12 (4) (2007), 044020.

[26] W. Xia, D. Piras, M. Heijblom, W. Steenbergen, T.G. van Leeuwen, S. Manohar, Poly(vinyl alcohol) gels as photoacoustic breast phantoms revisited, J. Biomed. Opt. 16 (7) (2011), 075002.

[27] A. Kharine, S. Manohar, R. Seeton, R.G.M. Kolkman, R.A. Bolt, W. Steenbergen, F. F.Md Mul, Poly(vinyl alcohol) gels for use as tissue phantoms in photoacoustic mammography, Phys. Med. Biol. 48 (3) (2003) 357–370.

[28] S. Manohar, A. Kharine, J.C. van Hespen, W. Steenbergen, T.G. van Leeuwen, Photoacoustic mammography laboratory prototype: imaging of breast tissue phantoms, J. Biomed. Opt. 9 (6) (2004) 1172–1181.

[29] M. Dantuma, S. Kruitwagen, J. Ortega-Julia, R.P. Pompe van Meerdervoort, S. Manohar, Tunable blood oxygenation in the vascular anatomy of a semi-anthropomorphic photoacoustic breast phantom, J. Biomed. Opt. 26 (3) (2021).

[30] A. Hariri, J. Palma-Chavez, K.A. Wear, T.J. Pfefer, J.V. Jokerst, W.C. Vogt, Polyacrylamide hydrogel phantoms for performance evaluation of multispectral photoacoustic imaging systems, Photoacoustics 22 (2021), 100245.

[31] F.T. D'Astous, F.S. Foster, Frequency dependence of ultrasound attenuation and backscatter in breast tissue, Ultrasound Med. Biol. 12 (10) (1986) 795–808.

[32] H.G. Nasief, I.M. Rosado-Mendez, J.A. Zagzebski, T.J. Hall, Acoustic properties of breast fat, J. Ultrasound Med. 34 (11) (2015) 2007–2016.

[33] J. Oudry, C. Bastard, V. Miette, R. Willinger, L. Sandrin, Copolymer-in-oil phantom materials for elastography, Ultrasound Med. Biol. 35 (7) (2009) 1185–1197.

[34] L.M. Cannon, A.J. Fagan, J.E. Browne, Novel tissue mimicking materials for high frequency breast ultrasound phantoms, Ultrasound Med. Biol. 37 (1) (2011) 122–135.

[35] F. Dong, E.L. Madsen, M.C. MacDonald, J.A. Zagzebski, Nonlinearity parameter for tissue-mimicking materials, Ultrasound Med. Biol. 25 (5) (1999) 831–838.

[36] K.V. Ramnarine, T. Anderson, P.R. Hoskins, Construction and geometric stability of physiological flow rate wall-less stenosis phantoms, Ultrasound Med. Biol. 27 (2) (2001) 245–250.

[37] E.L. Madsen, J.A. Zagzebski, G.R. Frank, An anthropomorphic ultrasound breast phantom containing intermediate-sized scatterers, Ultrasound Med. Biol. 8 (4) (1982) 381–392.

[38] W.D. D'Souza, E.L. Madsen, O. Unal, K.K. Vigen, G.R. Frank, B.R. Thomadsen, Tissue mimicking materials for a multi-imaging modality prostate phantom, Med. Phys. 28 (4) (2001) 688–700.

[39] S.R. Guntur, M.J. Choi, An improved tissue-mimicking polyacrylamide hydrogel phantom for visualizing thermal lesions with high-intensity focused ultrasound, Ultrasound Med. Biol. 40 (11) (2014) 2680–2691.

[40] J. Palma-Chavez, T.J. Pfefer, A. Agrawal, J.V. Jokerst, W.C. Vogt, Review of consensus test methods in medical imaging and current practices in photoacoustic image quality assessment, J. Biomed. Opt. 26 (9) (2021).

[41] Z. Guo, L. Li, L.V. Wang, On the speckle-free nature of photoacoustic tomography, Med. Phys. 36 (9) (2009) 4084–4088.

[42] W.C. Vogt, X. Zhou, R. Andriani, K.A. Wear, T.J. Pfefer, B.S. Garra, Photoacoustic oximetry imaging performance evaluation using dynamic blood flow phantoms with tunable oxygen saturation, Biomed. Opt. Express 10 (2) (2019) 449–464.

[43] W.C. Vogt, C. Jia, K.A. Wear, B.S. Garra, T.J. Pfefer, Phantom-based image quality test methods for photoacoustic imaging systems, J. Biomed. Opt. 22 (9) (2017) 1–14.

[44] A.M. Fales, W.C. Vogt, K.A. Wear, I.K. Ilev, T.J. Pfefer, Pulsed laser damage of gold nanorods in turbid media and its impact on multi-spectral photoacoustic imaging, Biomed. Opt. Express 10 (4) (2019) 1919–1934.

[45] Tools for assembling photoacoustic image quality test phantoms. [cited 2022; Available from: ⟨https://3dprint.nih.gov/discover/3DPX-016489⟩.

[46] J.L. Sandell, T.C. Zhu, A review of in-vivo optical properties of human tissues and its impact on PDT, J. Biophotonics 4 (11–12) (2011) 773–787.

[47] S.L. Jacques, Optical properties of biological tissues: a review, Phys. Med. Biol. 58 (11) (2013) R37–R61.

[48] P. Taroni, G. Quarto, A. Pifferi, F. Abbate, N. Balestreri, S. Menna, E. Cassano, R. Cubeddu, Breast tissue composition and its dependence on demographic risk factors for breast cancer: non-invasive assessment by time domain diffuse optical spectroscopy, PLoS One 10 (6) (2015), e0128941.

[49] F.S. Foster, J.W. Hunt, Transmission of ultrasound beams through human tissue–focusing and attenuation studies, Ultrasound Med. Biol. 5 (3) (1979) 257–268.

[50] L. Landini, R. Sarnelli, Evaluation of the attenuation coefficients in normal and pathological breast tissue, Med. Biol. Eng. Comput. 24 (3) (1986) 243–247.

[51] B. Malik, J. Klock, J. Wiskin, M. Lenox, Objective breast tissue image classification using Quantitative Transmission ultrasound tomography, Sci. Rep. 6 (2016) 38857.

[52] K. Nam, J.A. Zagzebski, T.J. Hall, Quantitative assessment of in vivo breast masses using ultrasound attenuation and backscatter, Ultrason Imaging 35 (2) (2013) 146–161.

[53] M. Zerhouni and M. Rachedine, Ultrasonic calibration material and method, US Patent 5,196,343, 1990.

[54] X. Zhang, C. Zhao, N. Xiang, W. Li, Chain entanglements and hydrogen bonds in carbopol microgel reinforced hydrogel, Macromol. Chem. Phys. 217 (19) (2016) 2139–2144.

[55] Daigle, R.E., Ultrasound imaging system with pixel-oriented processing, US Patent 8,287,456, 2006.

[56] American Association of Physicists in Medicine, AAPM Report No. 100 - Acceptance Testing and Quality Assurance Procedures for Magnetic Resonance

Imaging Facilities. 2010. https://www.aapm.org/pubs/reports/detail.asp?docid=101.
[57] International Electrotechnical Commission, IEC 61391–1:2006+AMD1:2017, Ultrasonics – Pulse-echo scanners – Part 1: Techniques for calibrating spatial measurement systems and measurement of system point-spread function response. 2017. https://webstore.iec.ch/publication/29057.
[58] Computerized Imaging Reference Systems, Inc., May 2021; Available from https://www.cirsinc.com/.
[59] M. Jaeger, J.C. Bamber, M. Frenz, Clutter elimination for deep clinical optoacoustic imaging using localised vibration tagging (LOVIT), Photoacoustics 1 (2) (2013) 19–29.
[60] G.L.G. Menezes, R.M. Pijnappel, C. Meeuwis, R. Bisschops, J. Veltman, P.T. Lavin, M.J. van de Vijver, R.M. Mann, Downgrading of breast masses suspicious for cancer by using optoacoustic breast imaging, Radiology 288 (2) (2018) 355–365.
[61] B.E. Dogan, G.L.G. Menezes, R.S. Butler, E.I. Neuschler, R. Aitchison, P.T. Lavin, F. L. Tucker, S.R. Grobmyer, P.M. Otto, A.T. Stavros, Optoacoustic imaging and gray-scale US features of breast cancers: correlation with molecular subtypes, Radiology 292 (3) (2019) 564–572.
[62] S. Hu, L.V. Wang, Photoacoustic imaging and characterization of the microvasculature, J. Biomed. Opt. 15 (1) (2010), 011101.
[63] W. Li, X. Chen, Gold nanoparticles for photoacoustic imaging, Nanomedicine 10 (2) (2015) 299–320.
[64] L.M. Neufeld, L.M. Larson, A. Kurpad, S. Mburu, R. Martorell, K.H. Brown, Hemoglobin concentration and anemia diagnosis in venous and capillary blood: biological basis and policy implications, Ann. N. Y Acad. Sci. 1450 (1) (2019) 172–189.
[65] M. Gassmann, H. Mairbaurl, L. Livshits, S. Seide, M. Hackbusch, M. Malczyk, S. Kraut, N.N. Gassmann, N. Weissmann, M.U. Muckenthaler, The increase in hemoglobin concentration with altitude varies among human populations, Ann. N. Y Acad. Sci. 1450 (1) (2019) 204–220.
[66] H.K. Walker, W.D. Hall, J.W. Hurst. Clinical Methods: The History, Physical and Laboratory Examinations, 3rd ed., Butterworth-Heinemann,, St. Louis, MO, 1990.

Jorge Palma-Chavez is a postdoctoral scholar in the in the Department of NanoEngineering at UC San Diego and a NSF Scholar-in-Residence fellow at FDA. Dr. Palma-Chavez graduated from Universidad La Salle in 2013 with a B.S. in Electrical Engineering. He earned his PhD in Biomedical Engineering from Texas A&M University, where he developed contrast agents for optical imaging techniques and designed vascular-targeted drug delivery platforms. He is currently working on tissue-mimicking phantoms for characterization and image quality assessment of photoacoustic imaging systems.

Keith A. Wear received his BA degree in applied physics from the University of California, San Diego and his MS and PhD degrees in applied physics from Stanford University. He is a research physicist at the FDA. He has served as associate editor in chief (2019-2021) and associate editor (2002-2021) of IEEE Transactions on Ultrasonics, Ferroelectrics, and Frequency Control. He is an associate editor of the Journal of the Acoustical Society of America and Ultrasonic Imaging. He is a fellow of the Acoustical Society of America, the American Institute for Medical and Biological Engineering, and the American Institute of Ultrasound in Medicine

Yash Mantri is a PhD candidate in the Bioengineering department at UC San Diego. He received his Btech. in Biomedical engineering from D.Y. Patil University in India. In the Jokerst lab he has developed activatable nanoparticle based sensors for reactive oxygen and nitrogen species (RONS), explored the fundamentals behind nanoparticle-based photoacoustic signal generation, and undertaken human clinical studies to monitor wound healing using photoacoustic imaging. He is currently studying the effects of blood pressure on photoacoustic signals and designing a colorimetric assay for COVID-19 detection.

Jesse V. Jokerst is a Professor in the Department of Nano-Engineering at UC San Diego. Dr. Jokerst graduated *cum laude* from Truman State University in 2003 with a B.S. in Chemistry and completed a Ph.D. in Chemistry at The University of Texas at Austin in 2009. Jesse was a postdoc at Stanford Radiology from 2009 to 2013 and was an Instructor in that same department from 2013 to 2015. Jesse started at UCSD in July of 2015, and he has received the NIH K99/R00 Pathway to Independence Award, the NIH New Innovator Award, the NSF CAREER Award, and Stanford Radiology Alumni of the Year Award. He is the PI of seven active NIH grants, three NSF grants, and serves on the Editorial Advisory Board of *ACS Applied Nano Materials* and *Nanoscale*.

William C. Vogt received his BS degree in mechanical engineering from the University of Massachusetts Amherst in 2009 and his PhD in biomedical engineering from Virginia Polytechnic Institute and State University in 2013. Since joining the FDA in 2013, he has been conducting regulatory science to develop tools and test methods for evaluating the safety and effectiveness of photoacoustic imaging devices. His research interests include photoacoustic imaging, tissue phantoms, nanoparticles, standardization, and biophotonic medical device characterization and evaluation.